# Automated cloud-drift winds from GOES images

Chandra Kambhamettu, K. Palaniappan and Frederick A. Hasler
Mesoscale Dynamics and Precipitation Branch
NASA Goddard Space Flight Center, Code 912
Greenbelt, MD 20771
chandra/palani/hasler@gloria.gsfc.nasa.gov, Tel: 301-286-5786, Fax: 301-286-1762

## ABSTRACT

Estimation of the atmospheric wind field based on cloud tracking using a time sequence of satellite imagery is an extremely challenging problem due to the complex dynamics of the imaging instruments and the underlying non-linear phenomena of cloud formation and weather. Cloud motion may involve both partial fluid motion and partial solid motion, which we model as semi-fluid motion. Motion algorithm with subpixel accuracy using differential geometry invariants of surfaces was developed to track clouds. The motion model is general enough to include both physical and geometrical constraints. Typically, a polynomial displacement function is used to model the local deformation behavior of a surface patch undergoing semi-fluid motion. The cloud tracking algorithm recovers local cloud surface deformations using a sequence of dense depth maps and corresponding intensity imagery, that captures the time evolution of cloud-top heights. Either intensity or depth information can be used by the semi-fluid motion analysis algorithm. A dense disparity or depth map that can be related to cloud-top heights is provided by the Goddard Automatic Stereo Analysis (ASA) module for input to the motion analysis module. The results of the automatic cloud tracking algorithm are extremely promising with errors comparable to manually tracked winds. Experiments were performed on GOES images of Hurricanes Frederic, Gilbert and Luis, and a temporally dense 1.5 minute time interval thunderstorm sequence covering Florida region. Future work involves using multispectral information, incorporating robustness, cloud motion segmentation and adaptive searching for improving operational cloud-tracking performance.

## 1 Introduction

The estimation of cloud-top structure and motion using multiple satellite views is an extremely challenging problem due to the complex dynamics of the imaging instruments and the underlying non-linear phenomena of cloud formation and weather. Accurate cloud heights and winds are important for a number of meteorological and climate applications [3, 10, 11, 1] such as cloud model verification, physically-based numerical weather prediction and data assimilation, and radiation balance estimation for Mission to Planet Earth type climate baseline studies. Stereoscopic multispectral measurement of cloud heights and time sequential estimation of cloud winds using geostationary and polar orbiting satellite-based instruments are essential because they provide information which is independent of other meteorological measurements.

The computational approach to cloud structure and motion estimation involves two primary modules [14]. The first module estimates stereo-based cloud structure using a hierarchical, multi-resolution coarse-to-fine search strategy with image warping at each level [15] and has been parallelized for the Maspar parallel machine having 16,384 processors. The second module estimates motion using a sequence of dense depth maps and corresponding intensity imagery, in order to capture the time evolution of cloud heights and has also been parallelized on Maspar parallel machine [12]. The IISS is a visualization tool that was developed for rapidly analyzing gigabyte-sized geophysical datasets [4], and was enhanced to visualize the results of the stereo analysis and semi-fluid motion estimation algorithms. This paper addresses motion

analysis part of our earlier work, which appeared in the *International Conference on Computer Vision '95* [14]. A brief overview of motion analysis for cloud tracking is presented next, followed by a description of the algorithms.

## 1.1 Motion Analysis

There can be two types of motions in general: *rigid* and *non-rigid* [8]. Cloud motion is a special case of non-rigid motion, where there is both partial fluid and partial solid motion, that we describe as being *semi-fluid motion*. The motion of objects exhibit a wide variation in behavior ranging from the simplest ideal frictionless rigid motion to the most complex turbulent fluid motion. Elastic motion deals with shape changes of continuous surfaces, and fluid motion deals with particle motion in which there is usually no continuity constraint among neighboring particles that are free to move according to the underlying dynamics. Although there has been an increasing amount of research in the individual categories of motion behavior, there have not been many attempts to combine different classes of motion models. In the fluid motion case when the local continuity of a surface is partially preserved, it should be advantageous to use both the characteristics of local continuity required for estimating surface properties, along with the flexibility of larger localized particle motion that would otherwise violate most local continuity assumptions. An ideal example of this category of motion, which we call *semi-fluid motion* is the non-rigid motion of clouds. Other examples may be found in the atmospheric sciences, as well as in hydrospheric modeling of ocean eddies and currents that mix and split thus maintaining some larger scale features identifiable in multi-spectral imagery, or biological cells that undergo fission or fusion processes. Time varying properties of clouds represent a prototypical example of semi-fluid motion behavior and offers a new experimental area for further investigation of non-rigid motion models.

We now present definitions of each motion type based on differential geometric variations during the motion [8]. Corresponding error measures are also presented, which can be used to estimate motion parameters and point correspondences for each nonrigid motion model. Error measure is represented by $\varepsilon_R$, which is expressed in terms of differential geometric parameters such as Gaussian curvature ($K$), mean curvature ($H$), Unit-normal ($n$), coefficients of first fundamental form ($E, F, G$) and Discriminant ($D$). Note that the parameters corresponding to the deformed surface are represented by primes such as $K'$ for Gaussian curvature, $n'$ for unit-normal etc. Each model is based on geometry only, and new motion models can be added to the list by forming more generic relationships. The reader is suggested to refer to [2] or any other related text for a detailed description of differential geometry.

**Rigid motion** preserves the 3-D distances between any two points in an object. The object does not stretch or bend; hence both mean curvature and Gaussian curvature on the surface of the object remains invariant.

$$\varepsilon_R = (K' - K)^2 + (H' - H)^2$$

**Isometric motion** is nonrigid motion which preserves lengths along the surface as well as angles between curves on the surface.

$$\varepsilon_R = (K' - K)^2$$

From the Figure 1.1, we can deduce that AB=A'B', AC=A'C' and $\theta = \theta'$ in this type of motion.

**Homothetic motion** is a uniform expansion or contraction of a surface, where stretching ($t$) is constant throughout the surface.
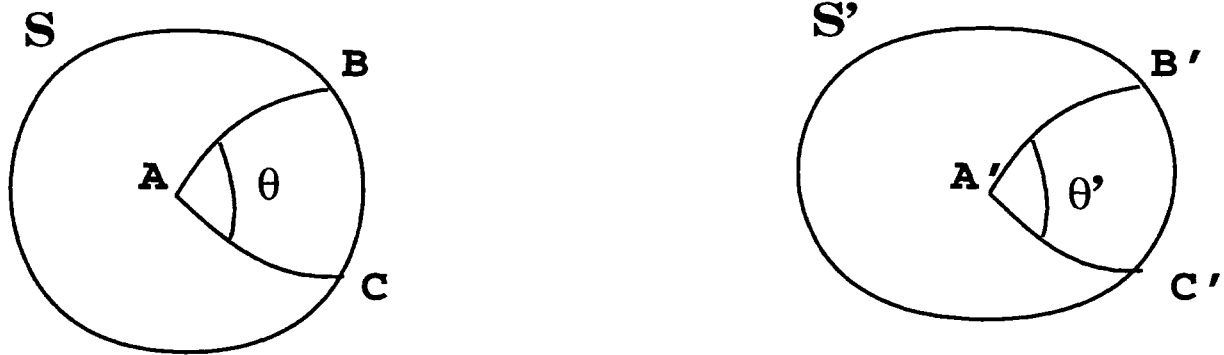
$$\varepsilon_R = (K't^2 - K)^2$$

Figure 1: Changes in Lengths and Angles Between Curves for Characterization of Nonrigid Motion Types

From the Figure 1.1, we have the ratio between the curves as constant, i.e, (AB/A'B' = AC/A'C' = constant), and also $\theta = \theta'$.

**Conformal motion** is nonrigid motion which preserves angles between curves on the surface during motion, but not lengths. Stretching $(t)$ is different at different points of the surface, however is same in different directions of any given point.

$$\varepsilon_R = (E' - t^2 E)^2 + (F' - t^2 F)^2 + (G' - t^2 G)^2$$

From the Figure 1.1, we can deduce that $\theta = \theta'$ in this type of motion.

**Elastic motion** is a nonrigid motion whose only constraint is some degree of continuity or smoothness. Motion at each point can be described by any polynomial function $s$. This kind of solid object motion is the most difficult to analyze. Following relations represent elastic motion when sufficiently small.

$$\varepsilon_R = (n' - n \times \mathbf{rot}s)^2 \quad \& \quad \varepsilon_R = (D' - D \mathrm{div}s)$$

**rot**$s$ can be defined as follows:

$$rot\ \mathbf{s} = \frac{1}{E}\mathbf{r}_1 \times \mathbf{s}_1 + \frac{1}{G}\mathbf{r}_2 \times \mathbf{s}_2.$$

where. $r$ is the position vector of a point, represented by $(u, v, z(u, v))$ and $E, G$ are the first fundamental coefficients. Note that the subscripts $1, 2$ indicate differentiation w.r.t to $u, v$ respectively.

**Semi-fluid motion** is a combination of elastic and fluid motion. This motion type will be elaborated more in coming sections.

**Fluid motion** is general nonrigid motion that need not be continuous. It may involve topological variations and turbulent deformations.

Each motion model presented above is a subset of the one at a higher level. Thus, the motion parameter becomes more generic as the complexity of the motion model used is increased. Input to these models can be a pair of range, intensity, or both types of images. In order to estimate point correspondence, error measure $(\varepsilon_R)$ is applied to each correspondence hypothesis over a template map. Each hypothesis

correspondence will then have a corresponding error measure, the minimum of which represents a good estimate for the correspondence. More than one correspondence can also be estimated with confidence measures for each hypothesis. $\varepsilon_R$ represents confidence measure when the underlying motion assumption is followed.

## 2 Automatic Motion Analysis

In this paper, we present a novel approach to estimate the point correspondences and motion parameters of a cloud element undergoing deformation. A unified algorithm having two approaches of motion analysis has been developed on the Maspar parallel machine. First approach utilizes a *continuous motion model*, where individual cloud elements under deformation are assumed to be continuous. Second approach assumes a *semi-fluid motion model*, where local continuity constraints are violated during deformation. Detailed description of the mathematical formulation used in these approaches is given below.

A local small deformation assumption can be used to derive relationships between unit-normals of a point on the surface before and after motion, and also between the curvatures at the point during deformation. We build on these derivations [16, 7] for automatic motion analysis of clouds. Consider a point defined parametrically as, $z(x, y)$, on a surface that undergoes small deformation changes and is transformed to the point $z'(x', y')$. The following relationship holds between the corresponding unit-normals [16, 7]:

$$\mathbf{n}' = \mathbf{n} - \mathbf{n} \times rot\ \mathbf{s} \tag{1}$$

where $\mathbf{n}$ corresponds to the unit-normal of a point before motion, and $\mathbf{n}'$ is the unit-normal of the same point after motion. The displacement function, $\mathbf{s}$ models the non-rigid motion of the local neighborhood or small patch around the point of interest and can be expressed in the imaging instrument coordinate system at the initial time step as,

$$\mathbf{s} = (x' - x, y' - y, z'(x', y') - z(x, y)). \tag{2}$$

The rotation or *curl* of the displacement function denoted as, $rot\ \mathbf{s}$ , is given by,

$$rot\ \mathbf{s} = \frac{1}{E}\mathbf{z}_1 \times \mathbf{s}_1 + \frac{1}{G}\mathbf{z}_2 \times \mathbf{s}_2. \tag{3}$$

The subscripts 1 and 2 indicate differentiation with respect to the parameters $x$ and $y$ respectively and the denominators, $E\ (= z_1 \cdot z_1)$ and $G\ (= z_2 \cdot z_2)$, are coefficients of the first fundamental form [16]. Polynomial functions are the simplest models for the local displacement function of a small patch undergoing small deformation. In our cloud-motion experiments, and in order to derive simple analytical relationships for differential geometry parameters, a small patch is assumed to undergo a local affine transformation defined as,

$$\mathbf{s}(x, y) = (a_i x + b_i y + c_i, a_j x + b_j y + c_j, a_k x + b_k y + c_k). \tag{4}$$

Let the unit-normal of a point before motion be defined as, $\mathbf{n} = (n_i, n_j, n_k)$ and the unit-normal of the same point after motion as, $\mathbf{n}' = (n'_i, n'_j, n'_k)$. Surface normals and other intrinsic surface properties are estimated by using locally fitted quadratic surfaces for each small patch though the relationship between the normals (1) holds for all surface models. From (1), (2), (3) and (4), the following linearly independent equations can be derived [7, 9]:

$$\left[ \frac{-n_k z_1}{E} a_i + \left( \frac{n_i - n_k z_2 - n_j}{G} \right) b_i + \left( \frac{n_j - n_k z_1 - n_i}{E} \right) a_j - \frac{n_k z_2}{G} b_j + \frac{n_k}{E} a_k + \frac{n_k}{G} b_k - n_i + n_i' - n_j + n_j' \right] = 0, \tag{5}$$

$$\left[\frac{n_i z_1}{E}a_i + \frac{n_i z_2}{G}b_i + \frac{n_j z_1}{E}a_j + \frac{n_j z_2}{G}b_j - \frac{n_i}{E}a_k - \frac{n_j}{G}b_k - n_k + n_k'\right] = 0. \tag{6}$$

The components of the displacement function, $s(\cdot)$, are the unknowns in the above equations. Although the displacement function has nine unknowns, Eq. (2) can be used to solve for the constant terms. Using (5) and (6) provides two independent constraints for each point correspondence, so three point correspondences are needed to solve for the six unknowns in the affine displacement model (4). Using just three point correspondences is not as reliable as the least squares minimization approach described next.

Since each small patch is assumed to experience small continuous deformations locally, the continuity constraint can be used to hypothesize a set of point correspondences or equivalently a template mapping $\eta_R$, between corresponding patches. The hypothesis point set or search area is defined as $L_R$ with the subscript $R$ used to indicate that the hypothesis testing is done using range or disparity data. The best match is the hypothesis which minimizes the total sum of the squared errors, given by (5) and (6) defined as $\varepsilon_{R_1}(x,y)$ and $\varepsilon_{R_2}(x,y)$ respectively,

$$\varepsilon_R(x,y) = \sum_{i \in \eta_R} \left(\varepsilon_{R_1}(x,y)\right)_i^2 + \left(\varepsilon_{R_2}(x,y)\right)_i^2. \tag{7}$$

The error function (7) can be minimized w.r.t each of the six unknowns, $(a_i, b_i, a_j, b_j, a_k, b_k)$, in the affine displacement function, resulting in six equations that can be solved using the hypothesized patch correspondence(s). Once $c_i, c_j, c_k$ are calculated using Eq. (2), the displacement function (4) for a local patch is completely specified. Using the estimated displacement function associated with each hypothesis the errors $\varepsilon_R(x,y)$ can be ranked. The matching hypothesis associated with the smallest error is assumed to represent the deformable motion.

The minimization procedure is suitable for locally continuous surfaces that have small deformations. However, it needs to be modified to include semi-fluid motion where the continuity constraint is relaxed locally. Intensity-based information is used to complement the matching process discussed above which relies primarily on local surface shape characteristics and depth analysis. The algorithm for semi-fluid motion analysis has three steps. The first step deals with determining a set of possible semi-fluid template mappings using intensity information for each local patch. The second step evaluates the error for each hypothesized correspondence provided by the template mapping and selects the most reliable semi-fluid mapping. The third step is to refine the motion parameters of the semi-fluid mapping to sub-pixel accuracy.

The neighborhood template mapping for $\eta_R$ can be continuous as shown in Fig. 2(a), or quite discontinuous under semi-fluid motion as shown in Fig. 2(b). Evaluating all possible semi-fluid template mappings between corresponding neighborhoods is combinatorially explosive. Determining the most plausible semi-fluid template mapping is made more tractable by using intensity information and tracking intensity features. For the cloud motion experiments, the discriminant was used as an intensity-based differential geometry parameter [9, 16]. The intensity-based algorithm allows small local regions within the template to undergo discontinuous semi-fluid motion. Other techniques such as optic flow-based segmentation that can be adapted to robustly estimate the local semi-fluid template mapping for motion tracking are also being investigated [5]. In order to determine the best semi-fluid mapping, Eq. (7) that measures the error in the surface or range normal constraint, is evaluated for each correspondence hypothesis using the semi-fluid template maps generated in the previous step. The error $\varepsilon_R(x,y)$ is computed within a small patch neighborhood for the pixel of interest and overlapping windows are used in computing the errors (5) and (6). The reliability in selecting the appropriate template mapping is improved by evaluating the error function over the entire neighborhood of points $(\eta_R)$, rather than at a single feature or individual pixel. The template mapping correspondence hypothesis with the minimum error is assumed to represent the best estimate of the local semi-fluid motion behavior. The total error $\varepsilon_R(x,y)$ can be used as a confidence
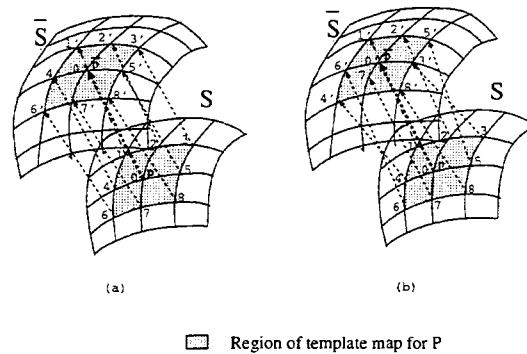
Figure 2: Local non-rigid deformation can be continuous as shown in the template mapping (a), or discontinuous under semi-fluid motion as shown in (b).

measure when the underlying motion assumption is valid. In our implementation, one can choose continuous, or semi-fluid motion model for cloud motion analysis. Figure 3 describes the processing steps of our algorithm as a flow chart. Semi-fluid motion tracking to sub-pixel accuracy is obtained by minimizing an energy function involving Gaussian curvature variations within the pixel. For a small patch defined by the vector function, $\mathbf{r}(x, y, z)$, that undergoes small deformation, the Gaussian curvatures before and after motion, $K$ and $K'$ respectively are related as [9],

$$K' = \frac{-1}{2D(1+\theta)}\left[\left(\frac{G + 2r_2 \cdot s_{21}}{D(1+\theta)}\right)_1 + \left(\frac{E + 2r_1 \cdot s_{12}}{D(1+\theta)}\right)_2\right]$$

$$= \frac{1}{(1+\theta)^2}K + f(x,y) \tag{8}$$

The discriminant (or infinitesimal area) at the point of interest is $D\ (= EG)$, and $\theta$ is the divergence or dilation at the same point. Dilation can be defined as the unit expansion/contraction of the feature during deformation and is expressed as,

$$\theta = div\ \mathbf{s} = \frac{1}{E}\mathbf{r}_1 \cdot \mathbf{s}_1 + \frac{1}{G}\mathbf{r}_2 \cdot \mathbf{s}_2 \ . \tag{9}$$

## 3  Experiments

Motion analysis experiments are performed on GOES images of Hurricanes Frederic, Gilbert and Luis, and a temporally dense 1.5 minute time interval thunderstorm sequence covering Florida region. In this section, we present the analysis of hurricanes Frederic and Luis, and Florida thunderstorm. The output of motion analysis algorithm (implemented on the Maspar) is a dense estimate of tracked fields on the cloud images. Thresholding based on local intensity variations is performed to filter out point tracks in non-cloudy regions. A local quadratic surface is fitted to estimate the various differential geometric measures that were used in the algorithm.

Figure 4 shows the thresholded particles that were tracked through the four frames of hurricane Frederic having a time interval of 7.5 minutes between each successive frame. Stereo of all the four frames are available from GOES-E and GOES-W satellites which subtend an angle of about 135° with respect to the center of the Earth providing a very large baseline for stereo analysis. Automatic stereo analysis was first performed on the stereo pairs to estimate the disparity. The estimated depth map time sequence

```
┌─────────────────────────────────────────┐
│   Acquire multi-view satellite imagery   │
└─────────────────────────────────────────┘
                    │
                    ▼
        ┌───────────────────────┐
        │  Stereo Analysis      │
        │  (Compute Disparity/  │
        │  Structure)           │
        └───────────────────────┘
                    │
                    ▼                         Semi-fluid
        ┌───────────────────────┐            motion model
        │  Set template size    │
        │  and search area      │────────────┐
        └───────────────────────┘            │
                    │                         ▼
         Continuous           ┌───────────────────────┐
         motion model         │  Discriminant-based   │
                              │  template mapping     │
                              │  (D = d - θ)          │
                              └───────────────────────┘
                    │                         │
                    ▼                         ▼
        ┌───────────────────────┐
        │  Surface patch-based  │
        │  matching using       │
        │  unit-normals         │
        │  (N = n - n X rots)   │
        └───────────────────────┘
                    │
                    ▼
        ┌───────────────────────┐
        │  Curvature-based      │
        │  subpixel matching    │
        │  (K = k + f(θ))       │
        └───────────────────────┘
                    │
                    ▼
                  ╭─────────╮
                 │ Visualization│
                 │  (IISS)      │
                  ╰─────────╯
```

Differential Geometric
Invariants:

k = Gaussian curvature at t1
k = Gaussian curvature at t2
n = Unit-normal at t1
N = Unit-normal at t2
d = Discriminant at t1
D = Discriminant at t2

Motion Parameters:

θ = Dilation
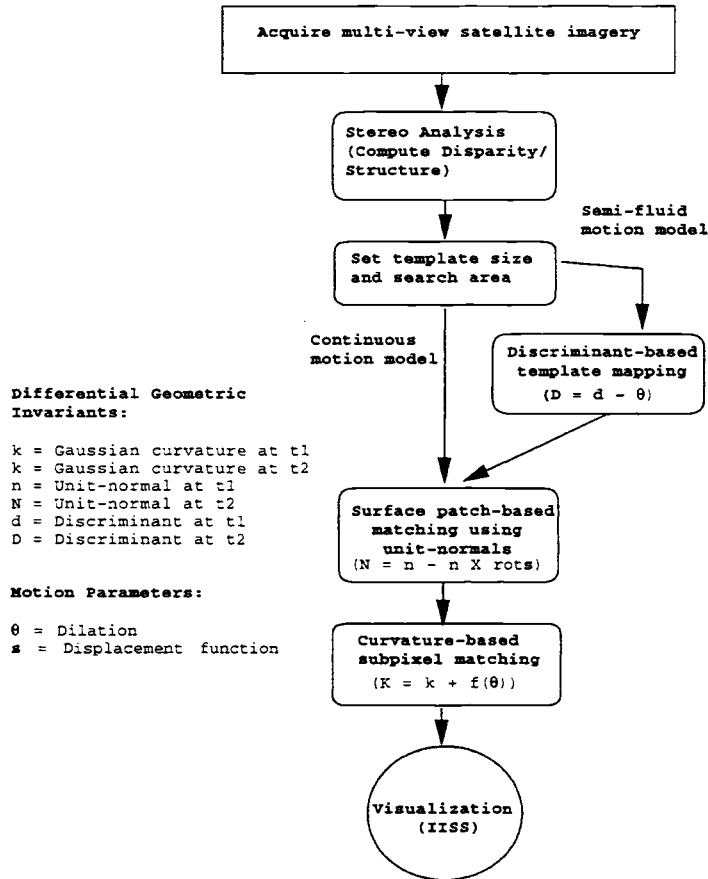s = Displacement function

Figure 3: Automatic Motion Analysis

along with corresponding intensity images from the eastern satellite were used to perform semi-fluid motion analysis. Since the time interval between frames is comparatively high, we perform semi-fluid motion analysis with larger template and search areas than those used for other data sets below (template=121X121, search=13X13).

Figure 5 shows the thresholded particles that were tracked in a Florida thunderstorm sequence. There are 49 image sequences of this data with a 1.5 minute time interval (stereo is not available). Top row represents the tracked results of a continuous motion model (template=11X11, search=9X9) applied to this data set, and the bottom row represents results generated by a semi-fluid motion model (template=11X11, search=9X9). Typically, it has been observed that continuous motion model estimates better tracks than semi-fluid model when the time interval is small; continuity constraints are preserved in short intervals.

Finally, motion analysis was performed on 490 frames of one-minute hurricane Luis data (10:23 UTC to 22:26 UTC, 06 Sep. 1995). Figure 6 depicts the thresholded particles that were tracked. Top row indicates the tracked particles at a given instant (1128 UTC), and the bottom row indicates tracked particles for the successive frame (1129 UTC). Continuous motion model (template=11X11, search=9X9) is used for the analysis, as the time interval is short enough so as to maintain continuity constraints of the cloud elements. Visualization of color-coded velocity tracks has also been generated for a qualitative assessment
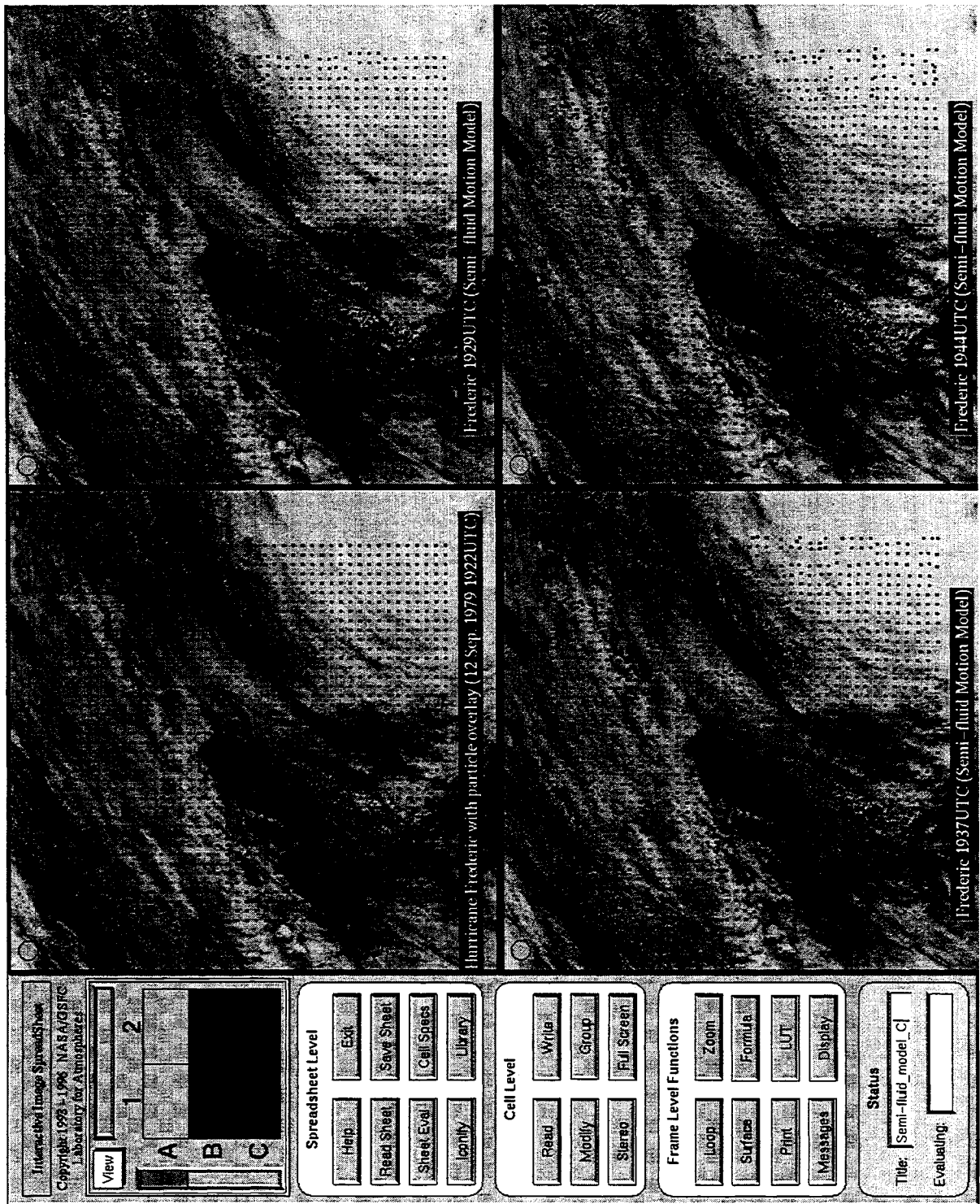
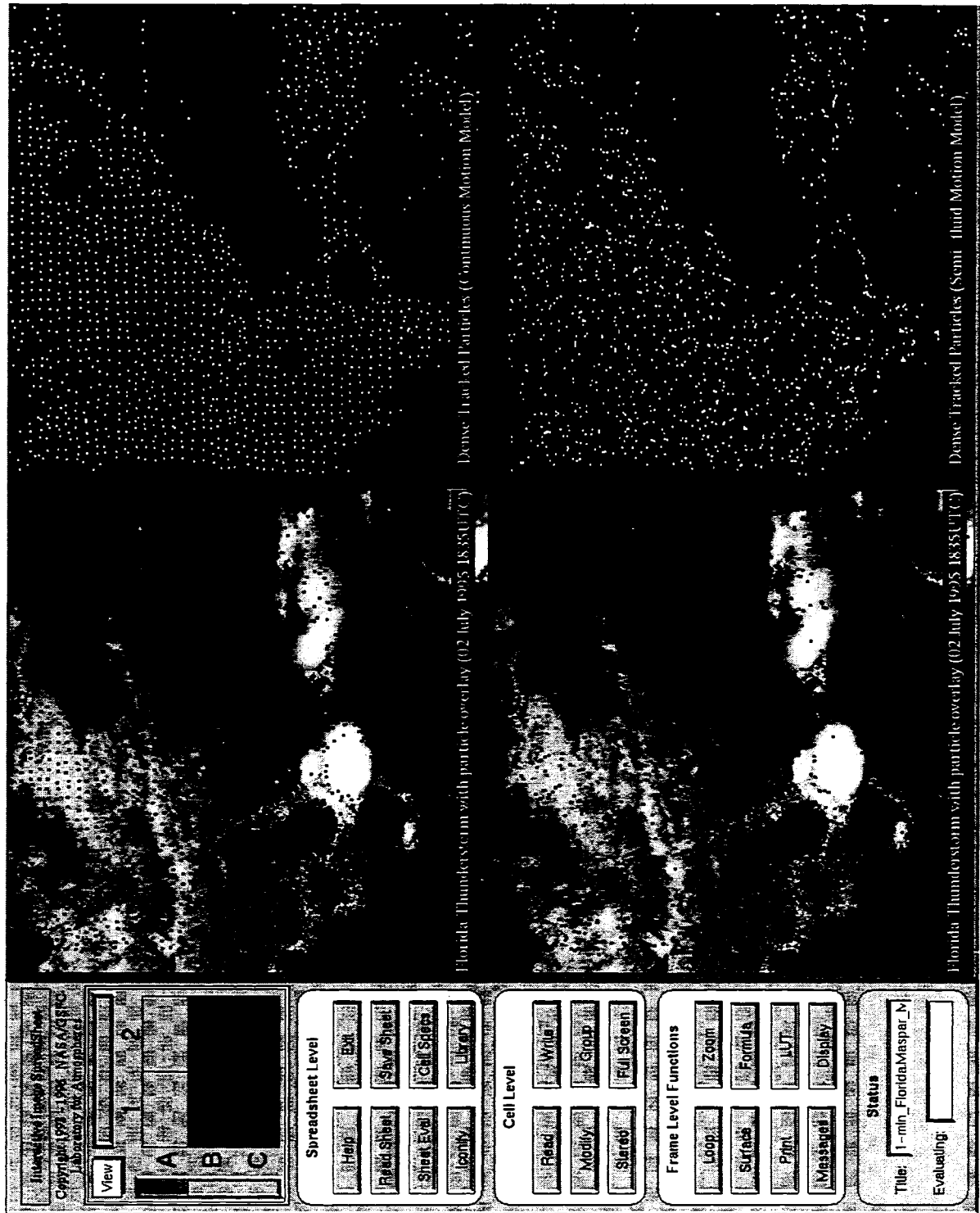Figure 4: Semi-fluid motion analysis of Hurricane Frederic

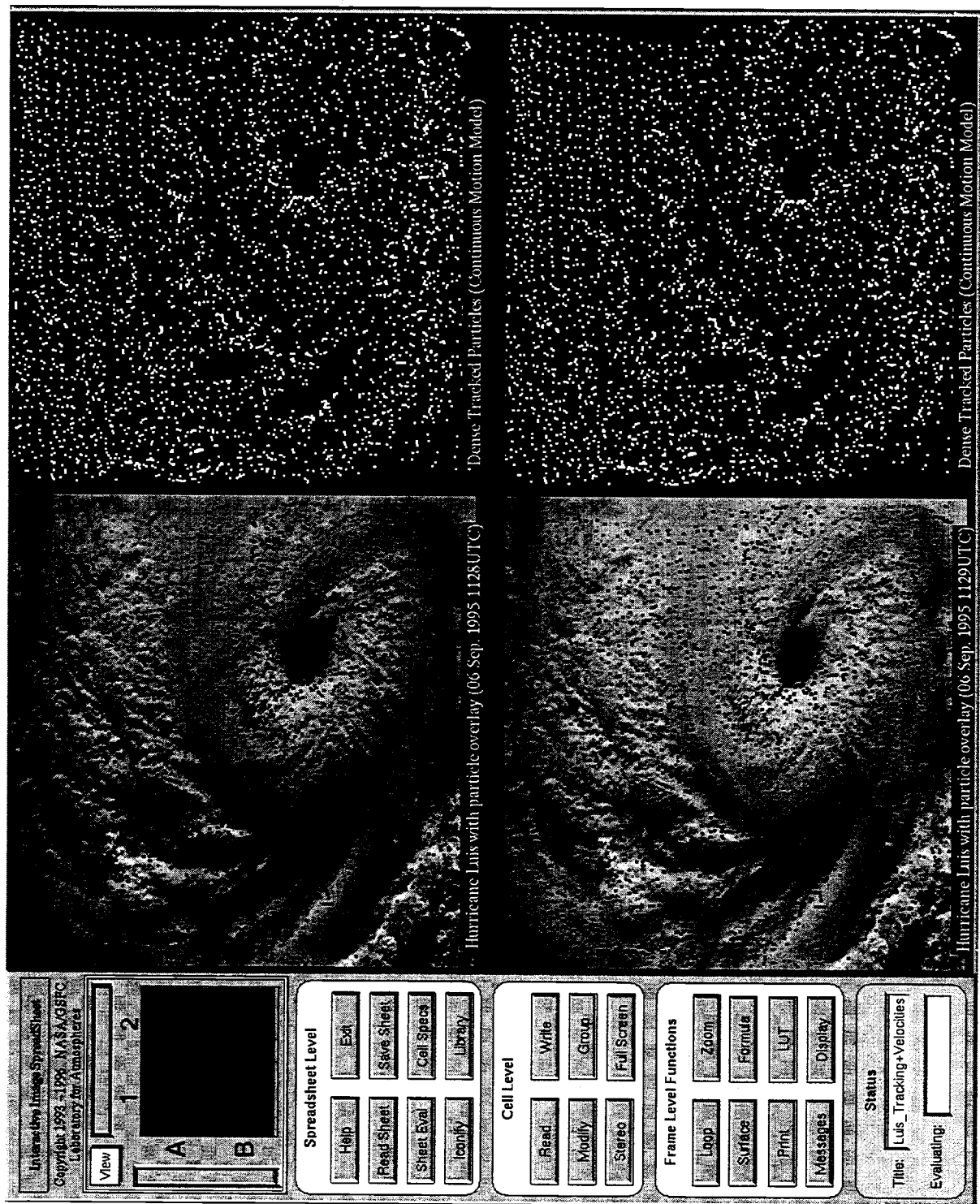Figure 5: Motion analysis of Florida Thunderstorm

Figure 6: Continuous motion analysis of Hurricane Luis

of the cloud-drift wind estimation. Please contact one of the authors to request for a corresponding video.

Validation of the cloud motion analysis is underway. So far, evaluation of the algorithm is performed by comparing the automatic tracking results with manual tracking analysis. An integrated system has been developed wherein the user can track a cloud element in a time sequence and immediately initiate the automatic tracking system. Cloud-drift winds can be generated from both the manual and automatic methods for validation. A complete statistical analysis of the tracked cloud-drift wind velocities can be obtained using the above mentioned system. Results thus far have been very promising, with RMS error as low as 5 mt/sec when well-defined cloud structures are being tracked. The algorithm fails when the cloud elements being tracked do not have structural variations or if there are multiple motions of clouds. We concentrate on this problem in our future direction, where cloud motion classification is performed before applying the motion model. A comprehensive error analysis of the algorithm in tracking different types of clouds is currently being performed.

## 4  Conclusions

We present a parallel algorithm for motion analysis that can produce dense motion fields (at every pixel) for a time-varying sequence. This algorithm has been implemented on the massively parallel Maspar computer. The algorithm can be applied to a pair of time-varying intensity data, surface or range data, or both intensity and surface data. A number of experiments using real satellite GOES imagery were performed. The algorithm produces favorable results compared to manually tracked cloud winds. However, additional validations are necessary for an operational performance of the algorithm in cloud-drift wind estimation.

Further research is needed to develop automatic parameter tuning methods for selecting optimum window sizes and various thresholds for different scenes using possibly machine learning methods. In addition to affine, higher-order polynomial and non-linear displacement functions guided by experiment can be used. Future work involves using adaptive hierarchical non-square template and search windows, using multispectral information, coupling stereo and motion estimation [6], improving the accuracy of the estimated motion field by using robust estimation [13], relaxation labeling or regularization, and post processing the motion field by using cloud classification.

## 5  Acknowledgements

## References

[1] G. G. Campbell, J. W. F. Purdom, and C. Vaughn. Cloud height and motion from multiple satellite observations. *SPIE*, August 1996.

[2] W. C. Graustein. *Differential Geometry*. Macmillan, New York, 1935.

[3] A. F. Hasler. Stereoscopic measurements. In P. K. Rao, S. J. Holms, R. K. Anderson, J. Winston, and P. Lehr, editors, *Weather Satellites: Systems, Data and Environmental Applications, Section VII-3*, pages 231–239. Amer. Meteor. Soc., Boston, MA, 1990.

[4] A. F. Hasler, K. Palaniappan, M. Manyin, and J. Dodge. A high performance interactive image spreadsheet (IISS). *Computers in Physics*, 8(3):325–342, 1994.

[5] Yan Huang, K. Palaniappan, Xinhua Zhuang, and Joe Cavanaugh. Optic flow field segmentation and motion estimation using a robust genetic partitioning algorithm. *IEEE Trans. Pattern Analysis and Machine Intelligence*, To be published.

[6] C. Kambhamettu, K. Palaniappan, and A. F. Hasler. Coupled, multi-resolution stereo and motion analysis. *IEEE International Symposium on Computer Vision*, pages 43–48, November 1995.

[7] Chandra Kambhamettu, Dmitry B. Goldgof, and Matthew He. Determination of motion parameters and estimation of point correspondences in small nonrigid deformations. *Proc. IEEE Conf. Computer Vision and Pattern Recognition*, pages 943–946, June 1994.

[8] Chandra Kambhamettu, Dmitry B. Goldgof, Demetri Terzopoulos, and Thomas S. Huang. Nonrigid motion analysis. In Tzay Young, editor, *Handbook of PRIP: Computer vision*, volume II, pages 405–430. Academic Press, San Diego, California, 1994.

[9] ChandraSekhar Kambhamettu. *Nonrigid Motion Analysis Under Small Deformations*. PhD thesis, University of South Florida, December 1994. Department of Computer Science and Engineering.

[10] Robert T. Merrill, W. Paul Menzel, Wayman Baker, James Lynch, and Eugene Legg. A report on the recent demonstration of NOAA's upgraded capability to derive cloud motion satellite winds. *Bull. American Meteorological Society*, 72(3):373–376, March 1991.

[11] S. J. Nieman. Goes-8/9 cloud drift winds. *SPIE*, August 1996.

[12] K. Palaniappan, M. Faisal, C. Kambhamettu, and A. F. Hasler. Implementation of an automatic semi-fluid motion analysis algorithm on a massively parallel computer. *IEEE International Parallel Processing Symposium*, pages 864–872, 1996.

[13] K. Palaniappan, Y. Huang, X. Zhuang, and A. F. Hasler. Robust stereo analysis. *IEEE International Symposium on Computer Vision*, pages 175–181, November 1995.

[14] K. Palaniappan, Chandra Kambhamettu, A. Frederick Hasler, and Dmitry B. Goldgof. Structure and semi-fluid motion analysis of stereoscopic satellite images for cloud tracking. *Proceedings of the International Conference on Computer Vision*, pages 659–665, 1995.

[15] H. K. Ramapriyan, J. P. Strong, Y. Hung, and C. W. Murray, Jr. Automated matching of pairs of SIR-B images for elevation mapping. *IEEE Trans. Geosciences and Remote Sensing*, 24(4):462–472, 1986.

[16] C. E. Weatherburn. *Differential Geometry in Three Dimensions*, volume II. Cambridge University Press, Cambridge, 1930.